




In the format provided by the authors and unedited.

Carbon star formation as seen through the non-monotonic initial–final mass relation

Paola Marigo ¹✉, Jeffrey D. Cummings², Jason Lee Curtis^{3,4}, Jason Kalirai^{5,6}, Yang Chen ¹, Pier-Emmanuel Tremblay⁷, Enrico Ramirez-Ruiz⁸, Pierre Bergeron⁹, Sara Bladh ^{1,10}, Alessandro Bressan ¹¹, Léo Girardi ¹², Giada Pastorelli ^{1,6}, Michele Trabucchi ^{1,13}, Sihao Cheng ², Bernhard Aringer ¹ and Piero Dal Tio ^{1,12}

¹Department of Physics and Astronomy G. Galilei, University of Padova, Padova, Italy. ²Center for Astrophysical Sciences, Johns Hopkins University, Baltimore, MD, USA. ³Department of Astrophysics, American Museum of Natural History, New York, NY, USA. ⁴Department of Astronomy, Columbia University, New York, NY, USA. ⁵Johns Hopkins University Applied Physics Laboratory, Laurel, MD, USA. ⁶Space Telescope Science Institute, Baltimore, MD, USA. ⁷Department of Physics, University of Warwick, Coventry, UK. ⁸Department of Astronomy and Astrophysics, University of California, Santa Cruz, CA, USA. ⁹Département de Physique, Université de Montréal, Montréal, Quebec, Canada. ¹⁰Theoretical Astrophysics, Department of Physics and Astronomy, Uppsala University, Uppsala, Sweden. ¹¹International School for Advanced Studies, Trieste, Italy. ¹²Astronomical Observatory of Padova - INAF, Padova, Italy. ¹³Department of Astronomy, University of Geneva, Versoix, Switzerland. ✉e-mail: paola.marigo@unipd.it

Supplementary Information

Carbon star formation as seen through the non-monotonic initial-final mass relation

Paola Marigo, Jeffrey D. Cummings, Jason Lee Curtis, Jason Kalirai, Yang Chen, Pier-Emmanuel Tremblay, Enrico Ramirez-Ruiz, Pierre Bergeron, Sara Bladh, Alessandro Bressan, Léo Girardi, Giada Pastorelli, Michele Trabucchi, Sihao Cheng, Bernhard Aringer, Piero Dal Tio

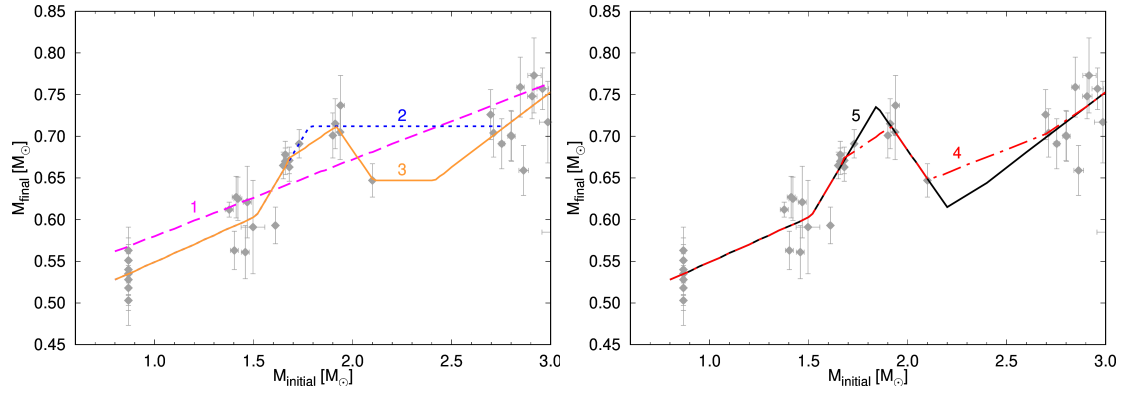
The WD mass distribution

The observed field-WD mass distribution (WDMD) in the MW can be employed to further check the impact of the IFMR kink and, more generally, of any assumed IFMR. Ideally, one may simultaneously use the observed IFMR data and the WDMD to constrain the coefficients of a parametric functional form expressing M_f as a function of M_i . However, at present the application of this method is made troublesome by the fact that a detailed consideration of the WDMD would introduce additional parameters to be examined, affecting both the population synthesis simulations (initial mass function, star formation history, chemical enrichment law) and the underlying stellar evolutionary models, in particular the metallicity dependence of all relevant processes involved (3DU and mass loss). This approach would introduce further uncertainties in our analysis with the consequence that the significance of our main observable, the IFMR, would be weakened. Therefore, at this stage, our strategy is to adopt the IFMR as the primary calibrator and employ the WDMD as an auxiliary verification tool to test the impact of different fitting forms. The fits examined here are illustrated in Supplementary Fig. 1. They adopt different assumptions concerning the IFMR kink and the behaviour of the IFMR through the region ($2.0 \lesssim M_i/M_\odot \lesssim 2.8$) that shows a substantial lack of data.

Supplementary Fig. 2 shows the resulting WDMDs for the five considered IFMR fits. All simulations were carried out with the TRILEGAL code,¹ assuming a Kroupa initial mass function,² an age-metallicity relation and a star formation history suitable for the MW disk. The stellar evolutionary tracks are taken from the PARSEC³ and COLIBRI^{4,5} databases, tailored to a grid of H-burning Post-AGB tracks and WD cooling sequences.⁶ Here we examine the distribution of WDs with masses from $0.55 M_\odot$ to $1.2 M_\odot$. We exclude WDs with $M_f < 0.55 M_\odot$ because their proper consideration would require taking care of various aspects that are still quite uncertain or go beyond the scope of this study, like the metallicity dependence of the IFMR (the metal-poor regime, in particular) and the effects of binary interactions. Within the considered mass range, the SDSS data⁷ has 4597 WDs of type DA with a signal-to-noise ratio > 10 . The simulated distributions were re-scaled to the same number of WDs as observed.

The simplest case (fit #1) corresponds to a monotonic relation that runs through the data over the range $0.8 \lesssim M_i/M_\odot \lesssim 3.1$. The monotonic representation has been the standard choice of all IFMR studies so far. This fit produces a rough approximation of the observations, but results in a WDMD peak located at too high mass, from $0.60 M_\odot$ to $0.65 M_\odot$ (Supplementary Fig. 2a). The shift is the consequence of the higher intercept we derive when attempting to describe the observed data through a single linear representation. This inconsistency, in addition to its poor representation of the IFMR data around $1.7 M_\odot - 2.0 M_\odot$ further argues against a simple monotonic fit.

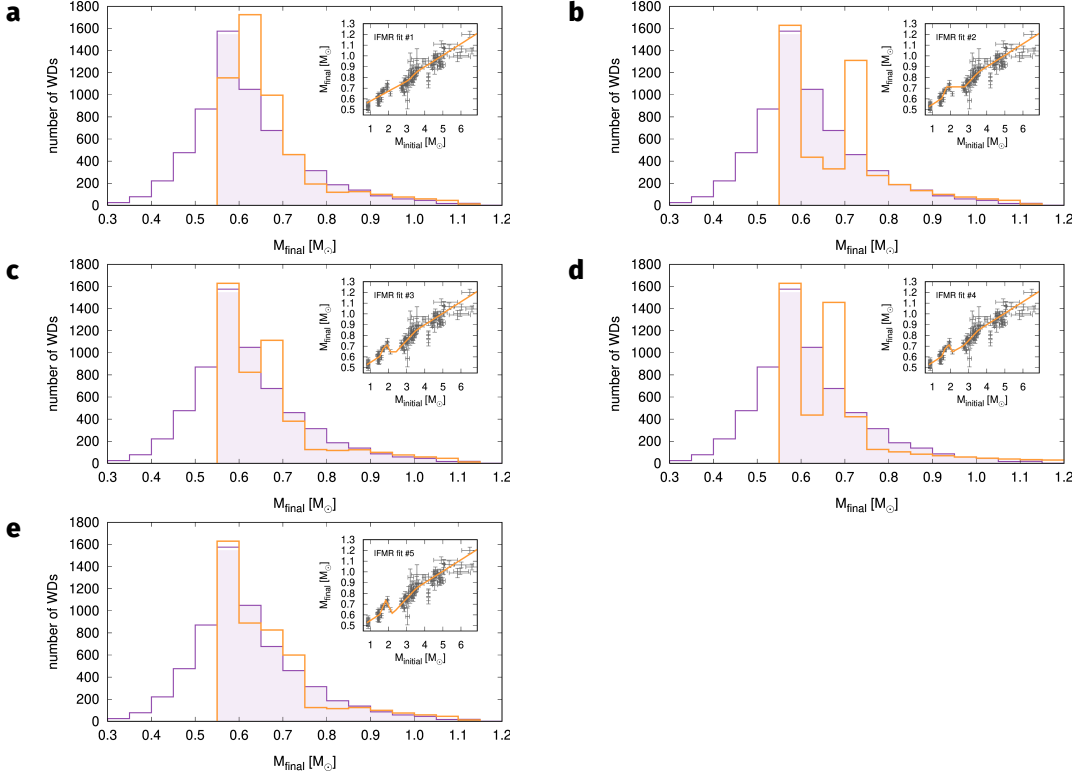
As next step we relax the monotonic assumption. We first fit the rising part of the IFMR up to a peak of $M_f \simeq 0.71 M_\odot$ located at $M_i \simeq 1.8 M_\odot$, and then, beyond it at larger M_i , we test a few trends. We start by adding a plateau (fit #2) of $M_f \simeq 0.71 M_\odot$ to join the increasing branch starting at $M_i \simeq 2.8 M_\odot$. In this way we exclude the WD belonging to NGC 752 from the fit. Clearly, the case #2 provides a very poor match of the whole observed WDMD from $M_f \simeq 0.6 M_\odot$ to $M_f \simeq 0.8 M_\odot$, with a dramatic excess of WDs of $M_f \approx 0.70 - 0.75 M_\odot$ (Supplementary Fig. 2b).



Supplementary Figure 1: Sample of five fitting relations compatible with the semi-empirical IFMR, which mainly differ in the description of the interval $1.7 \lesssim M_i/M_\odot \lesssim 2.8$. They are meant to explore the effect of introducing a non-monotonic feature in the IFMR, and to analyse its impact on the WDMD when varying the width and the amplitude of the associated kink. The error bars in the semi-empirical IFMR cover the range of $\pm 1 \sigma$.

Recognised that the plateau with $M_f \simeq 0.71 M_\odot$ over the range $1.8 \lesssim M_i/M_\odot \lesssim 2.8$ does not work, we reintroduce the NGC 752 data and impose that the fit #3 goes through the weighted averages of the WDs in the clusters over the interval $1.65 \lesssim M_i/M_\odot \lesssim 2.1$. After reaching a peak of $M_f \simeq 0.71 M_\odot$ at $M_i \simeq 1.91 M_\odot$, the fit #3 decreases down to recover the mass $M_f \simeq 0.65 M_\odot$ of N752-WD01 at $M_i \simeq 2.1 M_\odot$. From this point a small plateau with $M_f \simeq 0.65 M_\odot$ extends to $M_i \simeq 2.4 M_\odot$, where it intersects the extrapolated linear relation that describes the rising branch at larger masses ($M_i > 2.8 M_\odot$). Introducing this kink certainly improves the representation of the IFMR over the relevant M_i range, and at the same time it reduces the discrepancy in the WDMD that affects the previous plateau case (fit #2). We see that also the fit #3 yields an excess of WD with $M_f \simeq 0.65 - 0.70 M_\odot$, though at a lower level (Supplementary Fig. 2c).

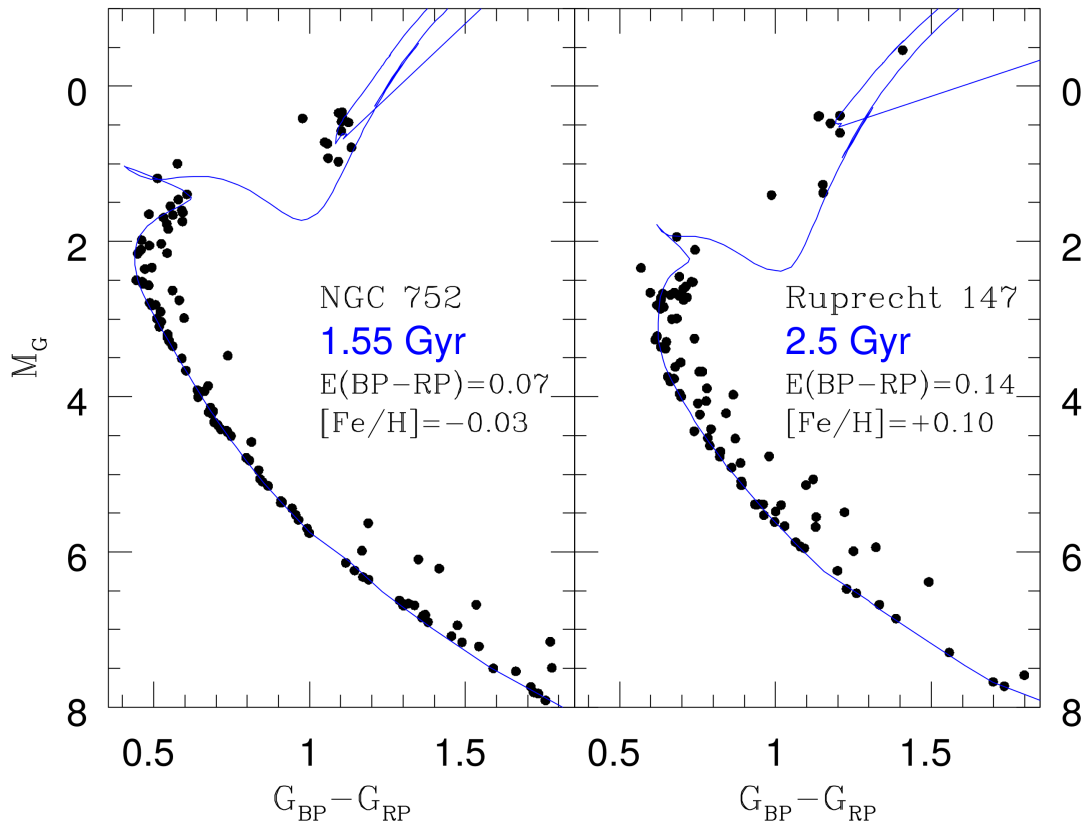
In the previous case (fit #3), we have tested the assumption that the IFMR stays flat over the range between $M_i \simeq 2.1 M_\odot$ and $M_i \simeq 2.4 M_\odot$, just where the IFMR is essentially unconstrained due to the lack of data. Therefore, we are driven to analyse other trends in this region. Now we examine the case (fit #4) in which, after reaching a minimum of $M_f \simeq 0.65 M_\odot$ in correspondence to N752-WD01, the IFMR regains a positive slope connecting to the branch starting at $M_i \simeq 2.8 M_\odot$. While the performance of the fit #4 is the same as the previous #3 – the two only differ in the region void of data –, the impact on the WDMD is sizeable. With the fit #4 the excess of WDs in the range $M_f \simeq 0.65 - 0.70 M_\odot$ appears now amplified (Supplementary Fig. 2d).



Supplementary Figure 2: The field white dwarf mass distribution in the MW. The observed distribution (purple histogram) is taken from the SDSS DR7.⁷ Over the range $0.55 \lesssim M_i/M_\odot \lesssim 1.2$ we overplot the results of population synthesis simulations (orange histograms) obtained assuming the same numbers of WDs as observed, and five different IFMR fits, shown in the insets and in Supplementary Fig. 1.

This fact leads us to increase the depth of the kink. With the fit #5 we assume that, after matching N752-WD01, the decrease continues down to a slightly deeper minimum ($M_f \simeq 0.62 M_\odot$ at $M_i \simeq 2.2 M_\odot$), beyond which a linear positive trend is re-established so as to pass through the data at intermediate M_i . In this way the surplus of WDs with $M_f \simeq 0.7 M_\odot$ is reduced to a satisfactory level. The resulting theoretical distribution much better matches the observed peak and approximately recovers the intermediate to high-mass wing (Supplementary Fig. 2e).

From the tests performed we conclude that a reasonably good reproduction of both the IFMR and the WDMD supports the existence of a kink in the IFMR. The decline that follows the peak at $M_i \simeq 1.8 - 1.9 M_\odot$ is needed to avoid the occurrence of a sizeable excess of WDs with $M_f \simeq 0.7 M_\odot$. Clearly, a more precise assessment of the extension (in M_i) and the amplitude (in M_f) of the kink will require further efforts involving additional observational data across the range $2.1 \lesssim M_i/M_\odot \lesssim 2.8$, coupled to a more detailed modelling of the WDMD. Future studies will be devoted to address these aspects.



Supplementary Figure 3: Colour-magnitude diagrams of the two old open clusters hosting the 7 newly discovered WDs. The cluster ages and reddenings of NGC 752 and Ruprecht 147 are fit using Gaia DR2 photometry, where only likely cluster members are displayed. The fit isochrones are the PARSEC v1.2S + COLIBRI PR17 isochrones^{3,8} with the adoption of the revised Gaia DR2 pass-bands.⁹ The cluster metallicities are derived from spectroscopic analyses in the literature,¹⁰⁻¹³ which reassuringly match well the main sequence trends and colours of the giants.

Other supporting evidence: Galactic semi-regular variables

Observed properties of Galactic AGB stars belonging to the class of semi-regular variables provide hints that support the proposed physical explanation. Let us examine the most relevant facts.

Progenitors of the IFMR kink. The picture proposed to explain the existence of the IFMR kink relies on the existence of carbon stars with small carbon enrichment and mild mass loss. In fact, Galactic carbon stars with low C – O (< 8.2) and low C/O (< 1.5) are observed,¹⁴ and have spectra dominated by dust-free stellar photospheres¹⁵ (see also Fig. 3, main article). They have moderate mass-loss rates¹⁶ (median value of $\simeq 2 \times 10^{-7} M_{\odot} \text{ yr}^{-1}$, not exceeding $10^{-6} M_{\odot} \text{ yr}^{-1}$, as well as low expansion velocities,¹⁶ typically with $v_{\text{exp}} < 10 \text{ km s}^{-1}$ (median value $\simeq 7 - 8 \text{ km s}^{-1}$). They are long-period variables,^{14,16} with pulsation periods $P < 400$ days (median value $\simeq 200$ days), mostly belonging to the classes of Irregulars (Lb) and Semi-regulars (Sra, Srb).

Overall, these facts converge to the conclusion that, as long as C/O remains low enough, carbon stars have weak winds, not sustained by radiation pressure on dust grains, but likely, by low-amplitude stellar pulsation.¹⁷⁻¹⁹

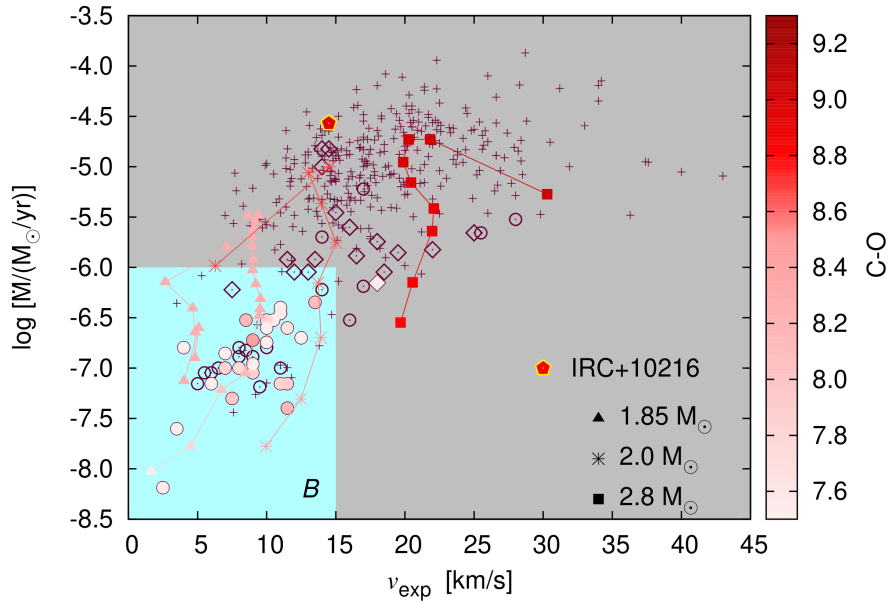
All the above-mentioned properties belong to the group of Galactic carbon stars inside the light blue region *B* of Supplementary Fig. 4 and, according to the proposed scenario, should also characterise the carbon-rich progenitors of the WDs we see now populating the IFMR kink. To better investigate this point we computed the evolution of the terminal wind velocity along a few selected TP-AGB tracks by means of a stationary AGB wind model,²⁰ which follows the growth of the dust grains as a function of stellar parameters (C/O, M , L , T_{eff} , \dot{M}). The adopted density profile across the circumstellar envelope was modified to include the effects of shocks in the inner wind.²¹ We see that the model with $M_i = 1.85 M_{\odot}$ spends most of its carbon-star phase inside or close to the region *B*, never exceeding $\dot{M} \simeq \text{few } 10^{-6} M_{\odot} \text{ yr}^{-1}$ and $v_{\text{exp}} \simeq 10 \text{ km s}^{-1}$. The predicted low values of the carbon excess are in agreement with the measured chemical abundances of this group of carbon stars.

These results support the proposed picture: the observed mild carbon enrichment and moderate mass loss, which define this sub-sample of SRV stars, set the suitable conditions for a prolongation of the carbon-star phase, hence for the growth of the core mass. We note that stellar models with larger initial masses ($M_i = 2.0 M_{\odot}$ and $M_i = 2.8 M_{\odot}$) may also cross the region *B*, but they soon leave it and attain larger carbon excess, as well as higher mass-loss rates and outflow velocities. Their properties are consistent with the group of infrared carbon stars, dominated by the presence of dust in their observed spectra,²² such as the well-known IRC+10126²³ which is characterised by $C/O \approx 2.5$, as inferred from molecular emission lines.²⁴

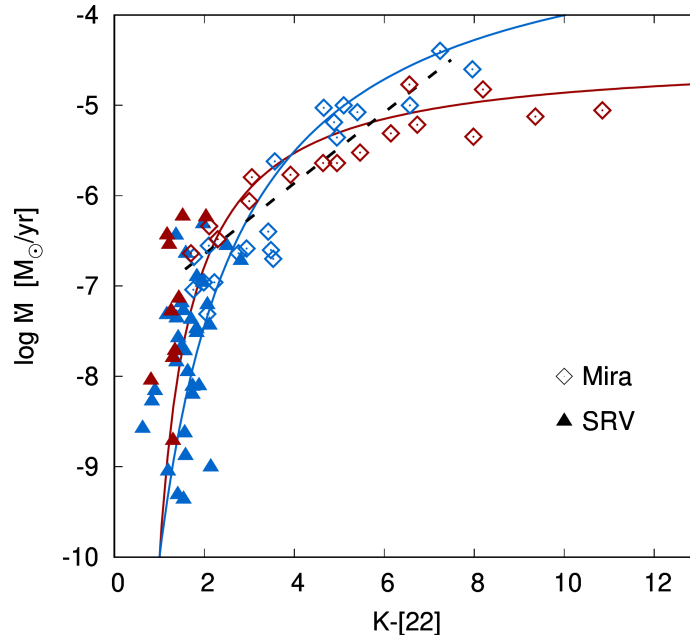
Mass loss of Galactic carbon stars. A closer look at the infrared properties of long-period variables in the Milky Way provides further support to the proposed mass-loss scenario for carbon stars.

To this aim it is useful to consider the colour $K - [22]$, where $[22]$ is the $22 \mu\text{m}$ band of the Wide-field Infrared Survey Explorer (WISE) space observatory.²⁵ As pointed out in a recent study,²⁶ the colour $K - [22]$ is an indicator of the mass-loss rate, as can be appreciated in Supplementary Fig. 6, which combines photometric data with recent mass-loss rate measurements, based on molecular line emission, for a group of MW long-period variables. We see a clear positive correlation between $K - [22]$ and \dot{M} . The SRVs mostly populate the branch steeply rising in mass-loss rate (\dot{M} up to $\approx 10^{-6} M_{\odot} \text{ yr}^{-1}$) characterised by low values of the infrared colour, up to $K - [22] \approx 3$. Then, the positive trend extends with the Mira stars which draw an elongated branch at larger mass-loss rates, reaching quite red colours, up to $K - [22] \approx 11$.

We fit the data of Supplementary Fig. 5 by adopting a functional form $y = a/(1 + b \times x) + c$, where $x = K - [22]$, $y = \log(\dot{M}_6)$ and \dot{M}_6 is the mass-loss rate in units of $10^{-6} M_{\odot} \text{ yr}^{-1}$. The coefficients of the best-fitting solutions are $a = -13.068$, $b = 0.814$, and $c = 3.205$ for M-type



Supplementary Figure 4: Mass-loss rates versus terminal wind velocities of Galactic intrinsic carbon stars. The observed data include a sample¹⁶ of optically-bright carbon stars (circles: Semi-regular and Irregular variables; diamonds: Mira variables) and an IR-complete sample²² (crosses). When the photospheric abundances of carbon and oxygen are available from spectroscopic analyses,^{14,27} the stars are colour-coded according to the carbon excess, $C - O$. The light-blue region (labelled with *B*) include Galactic carbon stars with low C/O and $C - O$, moderate \dot{M} and low v_{exp} , small-amplitude pulsation, mostly dust-free spectra. The median value of the measured carbon excess is $\simeq 7.5$, well below the threshold of dust-driven winds. Carbon stars outside the *B* region, such as the infrared carbon star IRC+10216 (pentagon), exhibit larger values of all these parameters (C/O , $C - O$, \dot{M} , v_{exp} , P), and their spectra are dominated by dust. For comparison, we overplot three evolutionary tracks during the carbon-star phase, with initial masses (in M_{\odot}) as indicated. The track with $M_i = 1.85 M_{\odot}$ and initial solar metallicity runs mostly within this region and exemplifies the evolution of the progenitor carbon stars that populate the IFMR kink with their WD remnants.



Supplementary Figure 5: Relation between the gas mass-loss rate and the infrared colour $K-[22]$ for a sample of MW semi-regular (triangles) and Mira variables (squares). Mass-loss measurements for Miras are taken from an extensive compilation of data,²⁶ but restricted to the most recent analyses.^{28–32} Data for SRVs are obtained from a new study³³ that employs DR2 Gaia distances.³⁴ Stars with spectral types M and C are coloured in blue and red, respectively. The solid lines are two fit relations with the same colour coding as for the data, the dashed line represents a linear fit (over the approximate range $1.5 \leq K - [22] \leq 7.5$) proposed in a recent work.²⁶

stars and $a = -4.036$, $b = 0.273$, and $c = 1.554$ for C-type stars. We use the two relations to colour a few evolutionary tracks and compare the results with observations of AGB variable stars in the diagram that relates the pulsation period with the infrared colour $K - [22]$ (Supplementary Fig. 6). Predicted periods for different radial models are obtained on the basis of an extensive theoretical work.³⁵ We apply the predicted fundamental period, P_0 , an empirical correction ($\log(P_0^{\text{cor}}) = \log(P_0) + 2.341 \times \log(T_{\text{eff}}) - 8.33$), which has shown to yield a satisfactory reproduction of the sequence C, mostly populated by Miras, in the period-luminosity diagram of the Small Magellanic Cloud.³⁶ In this respect it is worth underlining that the main focus here are the not the Mira variables but rather the SRVs, as is clear from the previous analyses on dust condensation (Fig. 3, main article), terminal wind velocities (Supplementary Fig. 4), as well as from the discussion that follows.

The diagram in Supplementary Fig. 6 is helpful to test the plausibility of the proposed mass-loss scenario, including the drop in mass loss during the very early stages of the C-star phase. The choice of the two evolutionary models with initial masses, $1.95 M_{\odot}$ and $2.40 M_{\odot}$, is motivated by the fact that the former should represent a stellar progenitor of the IFMR kink, while the latter exemplifies the case of a star which gets more efficiently enriched in carbon and populates the IFMR beyond the kink. We also note that the density of points along the tracks is controlled by the sampling of the pulse-cycle phase and it is not indicative of the observational probability, for which dedicated population synthesis simulations are necessary. In addition to our reference CDYN mass-loss prescription (Supplementary Figs. 6a–6b), we also consider TP-AGB models computed with the VW93 and B95 formulas, which do not depend explicitly on the carbon abundance (Supplementary Figs. 6c–6f).

Independently of the assumed mass loss, both TP-AGB tracks with $M_i = 1.95 M_{\odot}$ and $M_i = 2.4 M_{\odot}$ show a similar evolution of their pulsational properties. During the oxygen-rich stages (with $C/O < 1$) pulsation takes place in the 2nd and 1st overtone modes with periods $\lesssim 200$ days.

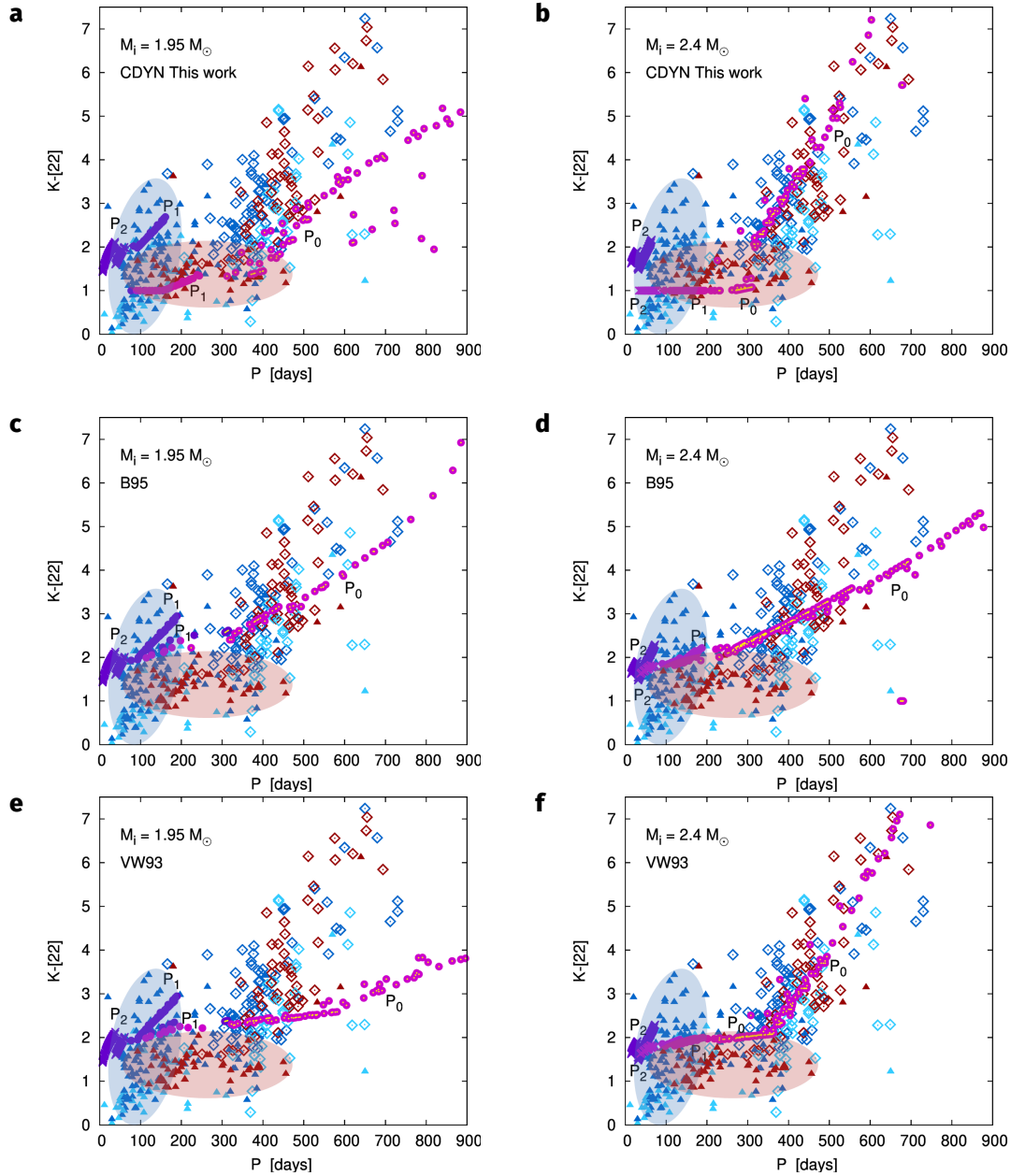
Soon after the transition to the C-star domain (with $C/O \gtrsim 1$), the evolution is initially still dominated by the 1st overtone modes, until when the fundamental mode becomes excited, remaining dominant up to the end of the quiescent TP-AGB evolution. Longer periods (typically $P_0 > 250$ days) are attained, the colour $K - [22]$ becomes redder and the models cross the sequence populated by the Miras. During these stage transitions back to higher overtone modes may take place along the same pulse cycle, typically when a star is in the post-flash low-luminosity dip.³⁵

While this picture holds, in general terms, for all the models shown in Supplementary Fig. 6, important differences emerge in the infrared colours $K - [22]$. During the $C/O < 1$ stages the models (purple) go through the region occupied by the M-type SRVs (blue ellipse). Their colour $K - [22]$ remains rather low, indication that the mass-loss rates are mostly moderate. Relatively red colours ($K - [22] \simeq 3$) are attained only by the $M_i = 1.95 M_\odot$ at the tip of its 1st overtone sequence, just before the transition to the carbon-star regime.

When the stars become carbon rich, the behaviour of the models radically differ depending on the assumed mass-loss scheme. Models that adopt the CDYN prescription (Supplementary Figs. 6a-6b) experience a drop in mass loss due to the low carbon excess and experience a temporary pulsation-driven moderate wind phase. The mass-loss drop translates into a colour jump: the model with $M_i = 1.95 M_\odot$ suddenly falls from $K - [22] \approx 3$ at the tip of the 1st overtone O-rich sequence down to $K - [22] \approx 1-2$, values that characterise the group of C-type SRVs (red ellipse). A similar behaviour, but with a less extended colour jump, is exhibited by the model with $M_i = 2.40 M_\odot$.

In summary, the CDYN models are able to reach the region of C-type SRVs as a consequence of the drop in mass loss predicted after the transition to the carbon-star phase. Later, as more TPs take place, the fundamental mode becomes dominant and the models attain larger mass-loss rates evolving through the branch mostly occupied by Mira stars at increasing period and redder $K - [22]$. We also note that the bottom of the fundamental-mode sequence is partly populated by SRVs.

Conversely, the VW93 and B95 models (Supplementary Figs. 6c-6f) do not recover the observed bluer $K - [22]$ colours characteristic of the C-type SRVs and remain outside the red ellipse. This implies that both prescriptions tend to overestimate the mass-loss rates during the early stages of the carbon-star evolution.



Supplementary Figure 6: Infrared colour $K - [22]$ vs pulsation period of AGB stars in the MW. Symbols denote different classes of variables (SRV: filled triangles; Mira: empty squares) while colours correspond to different spectral types (blue: M-type, cyan: S-type, red: C-type). The location of the bulk of M-type and C-type SRVs is highlighted with two elliptical shaded areas to help the comparison with the models. Here we include the results of TP-AGB evolutionary calculations for models with $M_i = 1.95 M_\odot$, $2.40 M_\odot$. Three descriptions of mass loss are adopted, namely the reference CDYN (a-b), B95 (c-d) and VW93 (e-f). The model results are shown for discrete values of the pulse-cycle phase ϕ (for each TP ϕ goes from 0.1 to 1 in steps of 0.1). Predicted periods as a function of stellar parameters are obtained from analytic relations³⁵ for different pulsation modes (cross: second overtone; filled circle: first overtone; filled circle with a yellow dot: fundamental mode), using a colour code that depends on the surface C/O (purple: C/O < 1, magenta: C/O > 1). The labels P_2 , P_1 , P_0 are placed close to the model sequences that share the same pulsation mode (second overtone, first overtone, and fundamental, respectively).

References

- ¹ L. Girardi, M. A. T. Groenewegen, E. Hatziminaoglou, and L. da Costa. Star counts in the Galaxy. Simulating from very deep to very shallow photometric surveys with the TRILEGAL code. *Astron. Astrophys.*, 436(3):895–915, Jun 2005.
- ² Pavel Kroupa. The Initial Mass Function of Stars: Evidence for Uniformity in Variable Systems. *Science*, 295(5552):82–91, Jan 2002.
- ³ A. Bressan, P. Marigo, L. Girardi, B. Salasnich, C. Dal Cero, S. Rubele, and A. Nanni. PARSEC: stellar tracks and isochrones with the PAdova and TRieste Stellar Evolution Code. *Mon. Not. R. Astron. Soc.*, 427:127–145, November 2012.
- ⁴ P. Marigo, A. Bressan, A. Nanni, L. Girardi, and M. L. Pumo. Evolution of thermally pulsing asymptotic giant branch stars - I. The COLIBRI code. *Mon. Not. R. Astron. Soc.*, 434:488–526, September 2013.
- ⁵ Giada Pastorelli, Paola Marigo, Léo Girardi, Yang Chen, Stefano Rubele, Michele Trabucchi, Bernhard Aringer, Sara Bladh, Alessandro Bressan, Josefina Montalbán, Martha L. Boyer, Julianne J. Dalcanton, Kjell Eriksson, Martin A. T. Groenewegen, Susanne Höfner, Thomas Lebzelter, Ambra Nanni, Philip Rosenfield, Peter R. Wood, and Maria-Rosa L. Cioni. Constraining the thermally-pulsing asymptotic giant branch phase with resolved stellar populations in the Small Magellanic Cloud. *arXiv e-prints*, page arXiv:1903.04499, Mar 2019.
- ⁶ Marcelo Miguel Miller Bertolami. New models for the evolution of post-asymptotic giant branch stars and central stars of planetary nebulae. *Astron. Astrophys.*, 588:A25, Apr 2016.
- ⁷ S. J. Kleinman, S. O. Kepler, D. Koester, Ingrid Pelisoli, Viviane Peçanha, A. Nitta, J. E. S. Costa, J. Krzesinski, P. Dufour, F. R. Lachapelle, P. Bergeron, Ching-Wa Yip, Hugh C. Harris, Daniel J. Eisenstein, L. Althaus, and A. Córscico. SDSS DR7 White Dwarf Catalog. *Astrophys. J. Suppl.*, 204(1):5, Jan 2013.
- ⁸ P. Marigo, L. Girardi, A. Bressan, P. Rosenfield, B. Aringer, Y. Chen, M. Dussin, A. Nanni, G. Pastorelli, T. S. Rodrigues, M. Trabucchi, S. Bladh, J. Dalcanton, M. A. T. Groenewegen, J. Montalbán, and P. R. Wood. A New Generation of PARSEC-COLIBRI Stellar Isochrones Including the TP-AGB Phase. *Astrophys. J.*, 835:77, January 2017.
- ⁹ M. Weiler. Revised Gaia Data Release 2 passbands. *Astron. Astrophys.*, 617:A138, October 2018.
- ¹⁰ J. L. Curtis, A. Wolfgang, J. T. Wright, J. M. Brewer, and J. A. Johnson. Ruprecht 147: The Oldest Nearby Open Cluster as a New Benchmark for Stellar Astrophysics. *AJ*, 145:134, May 2013.
- ¹¹ A. Bragaglia, X. Fu, A. Mucciarelli, G. Andreuzzi, and P. Donati. The chemical composition of the oldest nearby open cluster Ruprecht 147. *Astron. Astrophys.*, 619:A176, November 2018.
- ¹² R. M. Maderak, C. P. Deliyannis, J. R. King, and J. D. Cummings. WIYN Open Cluster Study. LVII. Oxygen Abundances of Solar-type Dwarfs in the Hyades and NGC 752. *AJ*, 146:143, December 2013.
- ¹³ B. A. Twarog, B. J. Anthony-Twarog, C. P. Deliyannis, and D. T. Thomas. A uvbyCaH β CCD Analysis of the Open Cluster Standard NGC 752. *AJ*, 150:134, October 2015.
- ¹⁴ D. L. Lambert, B. Gustafsson, K. Eriksson, and K. H. Hinkle. The chemical composition of carbon stars. I - Carbon, nitrogen, and oxygen in 30 cool carbon stars in the Galactic disk. *Astrophys. J. Suppl.*, 62:373–425, October 1986.
- ¹⁵ M. A. T. Groenewegen, L. B. van den Hoek, and T. de Jong. The evolution of galactic carbon stars. *Astron. Astrophys.*, 293:381–395, January 1995.

-
- ¹⁶ F. L. Schöier and H. Olofsson. Models of circumstellar molecular radio line emission. Mass loss rates for a sample of bright carbon stars. *Astron. Astrophys.*, 368:969–993, March 2001.
- ¹⁷ I. McDonald and M. Trabucchi. The onset of the AGB wind tied to a transition between sequences in the period-luminosity diagram. *Mon. Not. R. Astron. Soc.*, 484:4678–4682, April 2019.
- ¹⁸ I. McDonald, E. De Beck, A. A. Zijlstra, and E. Lagadec. Pulsation-triggered dust production by asymptotic giant branch stars. *Mon. Not. R. Astron. Soc.*, 481:4984–4999, December 2018.
- ¹⁹ J. M. Winters, T. Le Bertre, K. S. Jeong, C. Helling, and E. Sedlmayr. A systematic investigation of the mass loss mechanism in dust forming long-period variable stars. *Astron. Astrophys.*, 361:641–659, September 2000.
- ²⁰ A. S. Ferrarotti and H.-P. Gail. Composition and quantities of dust produced by AGB-stars and returned to the interstellar medium. *Astron. Astrophys.*, 447:553–576, February 2006.
- ²¹ P. Marigo, E. Ripamonti, A. Nanni, A. Bressan, and L. Girardi. Connecting the evolution of thermally pulsing asymptotic giant branch stars to the chemistry in their circumstellar envelopes - I. Hydrogen cyanide. *Mon. Not. R. Astron. Soc.*, 456:23–46, February 2016.
- ²² M. A. T. Groenewegen, T. de Jong, N. S. van der Bliek, S. Slijkhuis, and F. J. Willems. A flux-limited sample of galactic carbon stars. *Astron. Astrophys.*, 253:150–172, January 1992.
- ²³ M. Guélin, N. A. Patel, M. Bremer, J. Cernicharo, A. Castro-Carrizo, J. Pety, J. P. Fonfría, M. Agúndez, M. Santander-García, G. Quintana-Lacaci, L. Velilla Prieto, R. Blundell, and P. Thaddeus. IRC +10 216 in 3D: morphology of a TP-AGB star envelope. *Astron. Astrophys.*, 610:A4, February 2018.
- ²⁴ R. M. Mitchell and G. Robinson. The circumstellar dust shell of IRC + 10216. *Mon. Not. R. Astron. Soc.*, 190:669–682, March 1980.
- ²⁵ Edward L. Wright, Peter R. M. Eisenhardt, Amy K. Mainzer, Michael E. Ressler, Roc M. Cutri, Thomas Jarrett, J. Davy Kirkpatrick, Deborah Padgett, Robert S. McMillan, Michael Skrutskie, S. A. Stanford, Martin Cohen, Russell G. Walker, John C. Mather, David Leisawitz, III Gautier, Thomas N., Ian McLean, Dominic Benford, Carol J. Lonsdale, Andrew Blain, Bryan Mendez, William R. Irace, Valerie Duval, Fengchuan Liu, Don Royer, Ingolf Heinrichsen, Joan Howard, Mark Shannon, Martha Kendall, Amy L. Walsh, Mark Larsen, Joel G. Cardon, Scott Schick, Mark Schwalm, Mohamed Abid, Beth Fabinsky, Larry Naes, and Chao-Wei Tsai. The Wide-field Infrared Survey Explorer (WISE): Mission Description and Initial On-orbit Performance. *Astron. J.*, 140(6):1868–1881, December 2010.
- ²⁶ S. Uttenthaler, I. McDonald, K. Bernhard, S. Cristallo, and D. Gobrecht. Interplay between pulsation, mass loss, and third dredge-up: More about Miras with and without technetium. *Astron. Astrophys.*, 622:A120, February 2019.
- ²⁷ C. Abia, K. Cunha, S. Cristallo, and P. de Laverny. The origin of fluorine: abundances in AGB carbon stars revisited. *Astron. Astrophys.*, 581:A88, September 2015.
- ²⁸ S. Ramstedt, S. Mohamed, T. Olander, W. H. T. Vlemmings, T. Khouri, and S. Liljegren. CO envelope of the symbiotic star R Aquarii seen by ALMA. *Astron. Astrophys.*, 616:A61, August 2018.
- ²⁹ T. Danilovich, D. Teyssier, K. Justtanont, H. Olofsson, L. Cerrigone, V. Bujarrabal, J. Alcolea, J. Cernicharo, A. Castro-Carrizo, P. García-Lario, and A. Marston. New observations and models of circumstellar CO line emission of AGB stars in the Herschel SUCCESS programme. *Astron. Astrophys.*, 581:A60, September 2015.
- ³⁰ S. Ramstedt and H. Olofsson. The $^{12}\text{CO}/^{13}\text{CO}$ ratio in AGB stars of different chemical type. Connection to the $^{12}\text{C}/^{13}\text{C}$ ratio and the evolution along the AGB. *Astron. Astrophys.*, 566:A145, June 2014.

-
- ³¹ F. L. Schöier, S. Ramstedt, H. Olofsson, M. Lindqvist, J. H. Bieging, and K. B. Marvel. The abundance of HCN in circumstellar envelopes of AGB stars of different chemical type. *Astron. Astrophys.*, 550:A78, February 2013.
- ³² E. De Beck, L. Decin, A. de Koter, K. Justtanont, T. Verhoelst, F. Kemper, and K. M. Menten. Probing the mass-loss history of AGB and red supergiant stars from CO rotational line profiles. II. CO line survey of evolved stars: derivation of mass-loss rate formulae. *Astron. Astrophys.*, 523:A18, November 2010.
- ³³ J. J. Díaz-Luis, J. Alcolea, V. Bujarrabal, M. Santander-García, A. Castro-Carrizo, M. Gómez-Garrido, and J. F. Desmurs. Circumstellar envelopes of semi-regular long-period variables: mass-loss rate estimates and general model fitting of the molecular gas. *Astron. Astrophys.*, 629:A94, September 2019.
- ³⁴ Gaia Collaboration, A. G. A. Brown, A. Vallenari, T. Prusti, J. H. J. de Bruijne, C. Babusiaux, C. A. L. Bailer-Jones, M. Biermann, D. W. Evans, L. Eyer, and et al. Gaia Data Release 2. Summary of the contents and survey properties. *Astron. Astrophys.*, 616:A1, August 2018.
- ³⁵ Michele Trabucchi, Peter R. Wood, Josefina Montalbán, Paola Marigo, Giada Pastorelli, and Léo Girardi. Modelling long-period variables - I. A new grid of O-rich and C-rich pulsation models. *Mon. Not. R. Astron. Soc.*, 482(1):929–949, January 2019.
- ³⁶ G. Pastorelli. *Calibrating the Thermally-Pulsing Asymptotic Giant Branch Phase with resolved stellar populations in nearby galaxies*. PhD thesis, Padova University, March 2019.